The Electrochemical Society
Advancing solid state & electrochemical science & technology

Influence of NCM Particle Cracking on Kinetics of Lithium-Ion Batteries with Liquid or Solid Electrolyte

View the article online for updates and enhancements.

Joint International Meeting

PRiME 2020
October 4-9, 2020
Attendees register at NO COST!

PRiME
PACIFIC RIM MEETING
ON ELECTROCHEMICAL
AND SOLID STATE SCIENCE
2020

REGISTER NOW ▶

Influence of NCM Particle Cracking on Kinetics of Lithium-Ion Batteries with Liquid or Solid Electrolyte

Raffael Ruess,[1,2,z] Simon Schweidler,[3] Hendrik Hemmelmann,[1,2] Gioele Conforto,[1] Anja Bielefeld,[1,2,4] Dominik A. Weber,[4] Joachim Sann,[1,2] Matthias T. Elm,[1,2,5] and Jürgen Janek[1,2,3,*,z]

[1]*Institute of Physical Chemistry, Justus-Liebig-University Giessen, 35392 Giessen, Germany*
[2]*Center for Materials Research, Justus-Liebig-University Giessen, 35392 Giessen, Germany*
[3]*Battery and Electrochemistry Laboratory, Institute of Nanotechnology, Karlsruhe Institute of Technology (KIT), 76344 Eggenstein-Leopoldshafen, Germany*
[4]*Volkswagen AG, Group Innovation, 38440 Wolfsburg, Germany*
[5]*Institute of Experimental Physics I, Justus-Liebig-University Giessen, 35392 Giessen, Germany*

In liquid electrolyte-type lithium-ion batteries, Nickel-rich NCM ($Li_{1+x}(Ni_{1-y-z}Co_yMn_z)_{1-x}O_2$) as cathode active material allows for high discharge capacities and good material utilization, while solid-state batteries perform worse despite the past efforts in improving solid electrolyte conductivity and stability. In this work, we identify major reasons for this discrepancy by investigating the lithium transport kinetics in NCM-811 as typical Ni-rich material. During the first charge of battery half-cells, cracks form and are filled by the liquid electrolyte distributing inside the secondary particles of NCM. This drastically improves both the lithium chemical diffusion and charge transfer kinetics by increasing the electrochemically active surface area and reducing the effective particle size. Solid-state batteries are not affected by these cracks because of the mechanical rigidity of solid electrolytes. Hence, secondary particle cracking improves the initial charge and discharge kinetics of NCM in liquid electrolytes, while it degrades the corresponding kinetics in solid electrolytes. Accounting for these kinetic limitations by combining galvanostatic and potentiostatic discharge, we show that Coulombic efficiencies of about 89% at discharge capacities of about 173 mAh g_{NCM}^{-1} can be reached in solid-state battery half-cells with $LiNi_{0.8}Co_{0.1}Mn_{0.1}O_2$ as cathode active material and Li_6PS_5Cl as solid electrolyte.

List of symbols and abbreviations

A	electrochemically active electrode surface area
A_0	surface area of pristine electrode material
a_i	activity of component i
CC	current collector
C_a	capacitance at the anode|electrolyte interface
C_{dl}	capacitance at the cathode|electrolyte interface
C_{hf}	capacitance of high-frequency process
C_{int}	intercalation (differential) capacitance
c_0	equilibrium concentration of component i
c_i	concentration of component i
$\tilde{D}_i^f$	chemical diffusion coefficient of component i
$\tilde{D}_i^f$	chemical diffusion coefficient of component i determined using techniques based on finite diffusion
$\tilde{D}_i^{s-i}$	chemical diffusion coefficient of component i determined using techniques based on semi-infinite diffusion
$\tilde{D}_{LE}$	chemical diffusion coefficient in the liquid electrolyte
D_i^f	lattice diffusion coefficient of component i determined using techniques based on semi-infinite diffusion
F	Farady's constant
$f(V, t)$	potential- and time-dependent self-discharge
I	current
L	diffusion layer thickness
L^{LE}	diffusion layer thickness inside the liquid electrolyte
M_i	counter and reference electrode containing component i
n	number of transferred electrons
R	gas constant
R_0	resistance of ultra-high-frequency processes

R_a	charge-transfer resistance at the anode|electrolyte interface
R_{ct}	charge-transfer resistance at the cathode|electrolyte interface
$R_{D,i}$	diffusion resistance of component i
R_{hf}	resistance of high-frequency processes
$SSEl_i$	solid solution electrode that can dissolve component i
T	temperature
t	time during open-circuit-potential relaxation
t_d	duration of galvanostatic discharge
t_{pol}	duration of galvanostatic polarization pulse
V	potential
V_{OC}	open-circuit potential
$V_{OC}^{corr}(t)$	corrected open-circuit potential relaxation
$V_{OC}^f(t)$	open-circuit potential relaxation in case of finite diffusion
$V_{OC}^{s-i}(t)$	open-circuit potential relaxation in case of semi-infinite diffusion
W	enhancement factor
$Z_{D,i}$	diffusion impedance of component i
$Z_{D,LE}$	diffusion impedance of the liquid electrolyte
Z_W	Warburg coefficient
β_k, γ_k	electrode geometry related parameters
τ	relaxation time
τ_{app}	apparent relaxation time

Lithium-ion batteries (LIBs) have the potential to fulfill the increasing demands in electrochemical energy storage devices.[1,2] The transition from fossil fuels to regenerative power sources, especially for the emerging electric vehicles, poses numerous requirements for such LIBs.[1,2] Apart from a high energy density and the ability for fast charging, high safety, low cost and long cycle life are of particular importance, also under rough environmental conditions.[3] Substituting the liquid electrolyte in LIBs by a solid-state lithium-ion conductor, enabling the use of lithium metal as

*Electrochemical Society Member.
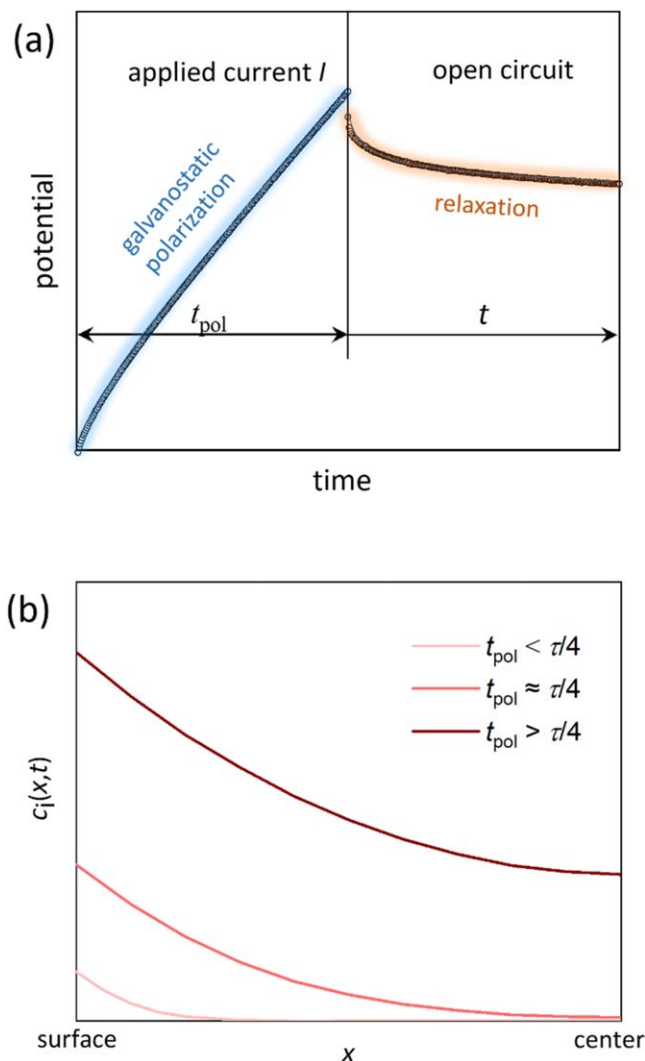zE-mail: raffael.ruess@phys.chemie.uni-giessen.de; juergen.janek@phys.chemie.uni-giessen.de

Figure 1. (a) Exemplary representation of a galvanostatic polarization and relaxation measurement. (b) Concentration gradient of mobile component i inside a particulate solid solution electrode after applying a galvanostatic discharging current for the polarization time t_{pol}. Calculated via Eq. 21 in Ref. 43.

active interface area between electrode and electrolyte can lead to kinetic limitations that could result in a low rate capability and low discharge capacity. Even for LEBs, it was revealed that slow kinetics limit the full utilization of active material.[24–27] Therefore, we feel motivated to investigate this aspect in ASSBs, too.

Consequently, in this work we investigate the lithium insertion and extraction kinetics in electrochemical half-cells with Ni-rich $LiNi_{0.8}Co_{0.1}Mn_{0.1}O_2$ (further only termed NCM for simplicity) as CAM, comparing liquid and solid electrolytes. If electrolytes with high ionic conductivity and anodes out of lithium-metal alloys are used, the internal resistivities associated with the cathode typically dominate.[10,28] Thus, we focus upon the kinetics of the cathode. Lithium ions need to be transferred between the electrolyte and the NCM and to be transported inside the NCM material. The exchange current density j_0 as well as the chemical diffusion coefficient $\tilde{D}_{Li}$ are characteristic for the respective rates and determine the internal resistivities that are directly influencing the discharge capacity.[29–31]

Experimentally measured diffusion coefficients for solid solution electrodes (including intercalation and insertion electrodes) vary by orders of magnitude even for nominally identical materials.[32–38] It has been shown that other relaxation processes in the cells, for example the interfacial electrode kinetics, strongly affect the measurement of $\tilde{D}_{Li}$.[37,39] Also, non-ideal electrode geometries that strongly influence surface area and diffusion length are discussed to influence the measurements.[38,40] Furthermore, self-diffusion has to be distinguished from chemical diffusion, since the former describes random lithium diffusion in an empty lattice while the latter includes the repulsive or attractive interaction of inserted and locally stored lithium and, therefore, has a different dependence on the state-of-charge (SOC).[41,42] In order to allow correct conclusions on the diffusion kinetics, we need to discuss beforehand system-related parameters that influence the measurement. Most important, we differentiate between semi-infinite and finite diffusion in order to distinguish diffusion on the short and the longer time scale. While the former describes diffusion near the sample surface, reflecting mostly surface-related material characteristics at short observation times, the latter relies on diffusion throughout the whole sample volume at longer observations times and depends on additional properties of the material. If the morphology of the electrode deviates from ideal geometries or the contacting is non-uniform, as it is mostly the case, significant differences between semi-infinite and finite diffusion kinetics are expected. To the best of our knowledge, this distinction has yet not been treated systematically for solid solution electrodes.

Most commonly, electrochemical small-signal methods are employed for the characterization of chemical diffusion, such as galvanostatic and potentiostatic intermittent transient techniques (GITT and PITT),[32–34,38–45] or electrochemical impedance spectroscopy (EIS)[32,40,44,46] and combinations of these.[37] In principle, all of these electrochemical small-signal methods are intrinsically connected via Fourier transformations, underlining that if basic conditions are fulfilled, all should deliver the same result with the same system-related uncertainties. In this work, we employ a galvanostatic polarization and relaxation technique and corroborate our results by EIS. We utilize and compare models for both semi-infinite and finite diffusion. The resulting diffusion coefficients are discussed in terms of structural and morphological properties of the investigated samples. In addition to the evaluation of diffusion kinetics, we analyze the charge transfer kinetics and develop an understanding of the chemo-mechanical evolution of the cathode during operation, which demonstrates the reasons for the inferior performance of typical NCM-based materials in ASSBs contrary to LEBs. We validate our results by charge-discharge measurements on electrochemical half-cells and reveal the detrimental effects of kinetic limitations on active material utilization as well as rate capability in ASSBs. However, by accounting for these kinetic limitations, we show that high discharge capacities are possible also in ASSBs with Ni-rich NCM as CAM and highlight that thiophosphate-based solid

anode, would promise to solve most of these issues.[4] As cathode active material (CAM), Ni-rich $Li_{1+x}(Ni_{1-y-z}Co_yMn_z)_{1-x}O_2$ (NCM or NMC) is considered superior to the classical $LiCoO_2$ because of the lower criticality of used elements and even higher energy density.[5,6] For lithium-ion batteries with liquid electrolyte (LEBs), NCM is a well-established CAM, achieving stable cycling at high currents and good utilization of active material.[7–9] However, its use in all solid-state batteries (ASSBs) has shown to be intricate.[10–13] Especially, if highly lithium-conductive sulfide- or thiophosphate-based solid electrolytes are used, stability, rate capability and discharge capacity is insufficient.[10–12,14–16] To prevent parasitic (electro)chemical side reactions at the solid electrolyte|NCM interface, protective coatings of NCM have widely been investigated and have shown to significantly improve cycling stability and discharge capacity.[15,17–19] However, the performance of NCM in ASSBs is still far away from corresponding LEBs, indicating more fundamental problems of this combination of materials.

As has been investigated in previous studies, apart from parasitic (electro)chemical side reactions, there are also mechanical aspects to be considered.[20–22] Volume changes in the electrodes upon (de)lithiation and the rigidity of solid electrolytes cause a loss of contact with the CAM during cell operation.[10,21,23] Changes in the electrochemically

electrolytes can efficiently be used even if their stability window is by far exceeded.

Methods

Determination of diffusion-related quantities by galvanostatic polarization and relaxation.—In the following we consider the general electrochemical cell CC|M$_i$|electrolyte|SSEl$_i$|CC with current collectors (CC), a counter and reference electrode (M$_i$) containing component i that has a constant chemical potential of i, an electrolyte conducting ions of component i, and a solid solution electrode that can dissolve component i (SSEl$_i$) by intercalation or insertion. From the solution of Fick's law under galvanostatic boundary conditions the concentration c_i of the diffusing species i at the surface of the solid solution electrode is obtained (Eq. 1) for an applied current I starting at $t_{pol} = 0$.[30,43] With c_0 being the equilibrium concentration of the component i, n is the number of transferred electrons, Faraday's constant F, the electrochemically active surface area A, the diffusion layer thickness L, $\tilde{D}_i$ the chemical diffusion coefficient of component i and the relaxation time constant $\tau = \frac{L^2}{\tilde{D}_i}$. γ_1, γ_2 and β_k are parameters depending on the electrode geometry with $\gamma_1 = 1$ or 3, $\gamma_2 = 1$ or 0.9 and $\beta_k = k\pi$ or the kth solution of the equation $\tan(\beta_k) = \beta_k$ for a flat plate or a spherical particle, respectively.[30]

$$c_i = c_0 + \frac{\gamma_1 I}{nFAL}t_{pol} + \frac{IL}{nFA\tilde{D}_i}\left[\frac{\gamma_2}{3} - 2\sum_{k=1}^{\infty}\frac{1}{\beta_k^2}\exp\left(-\beta_k^2\frac{t_{pol}}{\tau}\right)\right] \qquad [1]$$

Equation 1 includes the sum of two time-dependent functions. The linear part describes the filling or depletion of empty sites in the whole volume of the solid solution electrode (finite diffusion) and becomes significant for long polarization time t_{pol}. The part in the square brackets describes the expansion of the diffusion layer (semi-infinite diffusion) and is significant at short t_{pol}. The geometry-related constants γ_2 and β_k do not differ significantly between different geometries and, thus, the expansion of the diffusion layer is treated in good approximation as for a flat plate throughout the manuscript, disregarding its actual shape.[29]

Setting the applied current to zero after the polarization time t_{pol}, leads to an equilibration of the concentration c_i again over time. This equilibration can be measured as a relaxation of the open-circuit-potential $V_{OC}(t)$ of the solid solution electrode vs the counter electrode (Fig. 1a). If only small changes in c_0 are induced during the polarization step, $c_i(t)$ and $V_{OC}(t)$ are related by Eq. 2.[42]

$$V_{OC}(t) = V_0 - W\frac{RT}{nF}\frac{c_i(t) - c_0}{c_0} \qquad [2]$$

Hereby, W is the enhancement factor, which takes the form $W = \frac{\partial \ln(a_i)}{\partial \ln(c_i)}$ for a predominantly electronic conductor, with the activity a_i of dissolved component i in the solid solution electrode.[42] However, it has to be considered that different solutions for $V_{OC}(t)$ exist, depending on t_{pol}.[41] If t_{pol} is sufficiently long, so that the diffusion layer expands through the full electrode volume during the polarization step (Fig. 1b), the exponential function in Eq. 1 becomes negligible. The subsequent relaxation of $V_{OC}(t)$ (in the following termed as $V_{OC}^f(t)$ for the finite case) then contains information on both semi-infinite and finite diffusion.[41] This condition is fulfilled for $t_{pol} \geqslant \frac{\tau}{4}$.[41] In this case $V_{OC}^f(t)$ is given by Eq. 3, with the Warburg coefficient $Z_W = \frac{WRT}{n^2F^2Ac_0\sqrt{\tilde{D}_i}}$.[41,46]

$$V_{OC}^f(t) = V_0 - \frac{2}{\pi^2}IZ_W\sqrt{\tau}\sum_{k=1}^{\infty}\frac{1}{k^2}\exp\left(-k^2\pi^2\frac{t}{\tau}\right) \qquad [3]$$

However, if $t_{pol} < \frac{\tau}{4}$, the diffusion layer does not extend throughout the whole electrode volume and, consequently, $V_{OC}(t)$ only contains information about semi-finite diffusion (in the following termed as semi-infinite relaxation $V_{OC}^{s-i}(t)$) and is then

given by Eq. 4.[41] This relation is employed for the characterization of diffusion kinetics by the conventional galvanostatic intermittent titration technique (GITT).[42]

$$V_{OC}^{s-i}(t) = V_0 - \frac{2}{\sqrt{\pi}}IZ_W[\sqrt{t} - \sqrt{t_{pol} + t}] \qquad [4]$$

Both Eqs. 3 and 4 can be approximated for short relaxation times t by discarding 2nd and higher order terms leading to Eq. 5 for finite relaxation and Eq. 6 for semi-infinite relaxation, respectively.

$$V_{OC}^f(t) \cong V_0 - \frac{2}{\sqrt{\pi}}IZ_W\left[\sqrt{t} - \frac{t}{\sqrt{\tau}}\right] \qquad [5]$$

$$V_{OC}^{s-i}(t) \cong V_0 - \frac{2}{\sqrt{\pi}}IZ_W\left[-\sqrt{t_{pol}} + \sqrt{t} - \frac{t}{\sqrt{4t_{pol}}}\right] \qquad [6]$$

It is important to note that Eqs. 5 and 6 have the same time-dependent behavior and, thus, one could not reliably differentiate between a finite and a semi-infinite relaxation even from a good fit of the experimental data points. Furthermore, by comparing Eqs. 5 and 6 one can see that even if the condition $t_{pol} \geqslant \frac{\tau}{4}$ is not met and semi-infinite relaxation occurs, one would still obtain an apparent relaxation time constant $\tau_{app} = 4t_{pol}$ according to Eq. 5. This could then lead to the intriguing conclusion that the condition $t_{pol} \geqslant \frac{\tau}{4}$ would be met, leading to an underestimation of the actual value of τ and an overestimation of $\tilde{D}_i$. To avoid such pitfall, one has either to make sure that the experimentally determined τ_{app} is independent on t_{pol} or that $t_{pol} \gg \frac{\tau}{4}$. We emphasize that only negligible changes in c_0 are assumed to be induced during the polarization step, which means that the polarization current I has to be chosen in accordance to t_{pol}.

Another quantity of interest is the diffusion overpotential or resistance $R_{D,i}$ that adds up to the internal resistances (IR-drop) of a full electrochemical cell. By setting $t = 0$ in Eqs. 3 or 4 one obtains the diffusion overpotential during the polarization step, depending on either the passed polarization time t_{pol} for the semi-infinite case or the relaxation time τ for the finite case. We note that the diffusion overpotential does not significantly vary between both cases and can be generalized (Eq. 7) by using the experimentally accessible apparent relaxation time constant τ_{app}.

$$R_{D,i} = \frac{1}{I}V_{OC}^{s-i/f}(t = 0) \cong \frac{1}{3}Z_W\sqrt{\tau_{app}} \qquad [7]$$

Under real experimental conditions, the relaxation of $V_{OC}(t)$ of a solid solution electrode is not exclusively caused by the equilibration of the concentration gradient within the material, but has several influences that superimpose diffusion-related response. Most prominently, RC-relaxation of other sample-internal resistances and capacitances, such as e.g. interfacial charge-transfer resistances and double-layer capacitances, or chemical diffusion of the conducting salt in the liquid electrolyte play a role in the short time scale of $V_{OC}(t)$. These effects are revisited and discussed later in this work. However, also on the long time scale $V_{OC}(t)$ can be influenced by additional effects, which we will further subsume as self-discharge $f(V, t)$ (Eq. 8).

$$V_{OC}(t) = V_{OC}^{s-i/f}(t) + f(V, t) \qquad [8]$$

These effects involve e. g. the electronic conduction of the electrolyte, redox shuttle effects or parasitic side reactions at the surface of the solid solution electrode. In good approximation $f(V, t)$ goes linear with time and can take values up to some tens of mV per day for typical materials.[47] Such slow processes would then interfere mostly with the linear (finite diffusion) part of $V_{OC}^{s-i/f}(t)$, leading to an error in the determination of the relaxation time τ_{app}. To circumvent such error, one can exploit that the sign of

$V_{OC}^{s\text{-}i/f}(t)$ depends on the direction of the preceding polarization current, while $f(V, t)$ only depends on the potential of the electrode. Therefore, if a relaxation measurement $V_{OC}^{s\text{-}i/f}(t)$ after galvanostatic polarization with current I is followed by a second relaxation measurement $V_{OC}^{s\text{-}i/f}(t)$ with opposite direction of the polarization current, one can eliminate the parasitic effect of self-discharge by subtraction of both relaxation curves according to Eq. 9 retaining the corrected potential relaxation $V_{OC}^{corr}(I, t)$ (see Fig. SI-1 is available online at stacks.iop.org/JES/167/100532/mmedia), assuming $f(V, t)$ does not significantly alter during the measurement. This will allow a precise determination of long relaxation times τ_{app}. On the other hand, $f(V, t)$ can be isolated by addition of $V_{OC}^{s\text{-}i/f}(I, t)$ and $V_{OC}^{s\text{-}i/f}(-I, t)$).

$$V_{OC}^{corr}(I, t) = 2V_{OC}^{s\text{-}i/f}(I, t)$$
$$= V_{OC}^{s\text{-}i/f}(I, t) + f(V, t)$$
$$- [V_{OC}^{s\text{-}i/f}(-I, t) + f(V, t)] \qquad [9]$$

Overall, the presented galvanostatic polarization and relaxation method enables the measurement of the chemical diffusion coefficient $\tilde{D}_i$ of component i in solid solution electrodes from the Warburg coefficient Z_W (semi-infinite diffusion) and also provides access to the relaxation time constant τ which allows separate characterization of finite and semi-infinite diffusion. To the best of our knowledge, this rigorous formal analysis has not been reported before.

Electrochemical impedance spectroscopy.—In this work, electrochemical impedance spectroscopy is used to find the appropriate time scale for which the electrochemical response of the cell is dominated by diffusion inside the solid solution electrode, to support the galvanostatic polarization and relaxation experiments and also to quantify interfacial charge-transfer related properties of the solid solution electrode. The solid solution electrode is modelled by a generalized Frumkin and Melik-Gaykazyan (FMG) impedance element that accounts for interfacial charge-transfer (R_{ct}, C_{dl}), diffusion ($Z_{D,i}$) and storage (C_{int}) inside the material.[40,48] Despite the formally correct treatment of solid-state diffusion by a finite-space Warburg element, we chose the FMG-model since it accounts for a non-uniform particle size and, thus, allows improved fitting of real electrodes.[40,49] Other elements in the equivalent circuit are related to diffusion in the liquid electrolyte ($Z_{D,LE}$), charge-transfer at the anode (R_a, C_a), a high-frequency arc that incorporates contact or grain-boundary resistances (R_{hf}, C_{hf}) and a resistor R_0 that accounts for ultra-high frequency effects such as mainly migration in the solid electrolyte and electric resistances of the current collectors.[50,51] The equivalent circuit shown in Fig. 2 is used for all investigated cells, but some elements are discarded for individual cells, e.g. $Z_{D,LE}$ is neglected if a solid electrolyte is used.

Experimental

Sample preparation.—Commercial NCM powder (LiNi$_{0.8}$Co$_{0.1}$Mn$_{0.1}$O$_2$) was provided by Volkswagen AG with an average

secondary particle radius of $\sim 3\,\mu m$ and a specific surface area of $\sim 0.2\,m^2\,g^{-1}$ (determined by Kr-physisorption BET isotherm). Li$_6$PS$_5$Cl solid electrolyte powder was purchased from NEI. Prior to use, both powders were dried overnight in a Büchi oven at 200 °C under vacuum and transferred into an Ar-filled glovebox for further usage.

Electrochemical half-cells with liquid electrolyte (LEB) were prepared in a coin-cell-type arrangement. Cathodes were printed on aluminum foil from a slurry consisting of 90 wt% NCM, 5 wt% polyvinylidene difluoride binder (Solef 5130 PVDF, Solvay) and 5 wt% carbon (Super P, TIMCAL) in N-methyl pyrrolidone (Sigma-Aldrich). Subsequently, the electrodes were dried overnight in a Büchi oven at 120 °C under vacuum. CR2032 coin-type half-cells were assembled inside an Ar-filled glovebox by sequentially stacking the cathode sheet (14 mg of active material, Ø 12 mm), a GF/A glass microfiber separator (thickness 0.26 mm, Ø 17 mm, Whatman) and the Li-metal anode (thickness 1 mm, Ø 15 mm, Albemarle Germany GmbH). 50 μl LP47 (1 M LiPF$_6$ in a 3:7 mixture (wt:wt) of ethylene carbonate and diethyl carbonate were poured on top of the separator.

Electrochemical half-cells with solid electrolyte (ASSB) were prepared in a press cell-type arrangement. Details on the cell setup have been reported elsewhere.[28] Cathode composites were thoroughly mixed by hand grinding 70 wt% NCM and 30 wt% Li$_6$PS$_5$Cl (corresponding to a volume ratio of 46:54) inside an Ar-filled glovebox. We avoided the use of conductive carbon in the composite since it is a major source of degradation for thiophosphate-based solid electrolytes.[52] Cells were assembled by stacking 12 mg of cathode composite and 60 mg of Li$_6$PS$_5$Cl as separator, followed by uniaxially pressing with 30 kN (~ 380 MPa). The resulting pellet had a diameter of 10 mm and a thickness of approximately 470 μm (420 μm separator and 50 μm cathode composite) and the residual porosity of the cathode composite was measured to be around 14%. Afterwards, an indium foil (thickness 100 μm, Ø 9 mm) and a lithium foil (thickness 100 μm, Ø 6 mm) were added to the stack. A pressure of ~ 70 MPa was applied, which was maintained during electrochemical tests.

Electrochemical half-cells with liquid electrolyte and thin-film cathode (TF-LEB) were prepared in a pouch cell-type arrangement. Thin films of LiNi$_{0.33}$Co$_{0.33}$Mn$_{0.33}$O$_2$ were deposited by a sol-gel technique. Details on the preparation will be reported elsewhere.[53] Pouch-type cells were assembled inside an Ar-filled glovebox by sequentially stacking the thin film-coated substrate (180 μg of active material, geometrical surface area of 0.8 cm^2, film thickness 350 nm), the GF/A glass microfiber separator and the Li metal foil. 50 μl LP30 (1 M LiPF$_6$ in a 1:1 mixture (wt:wt) of ethylene carbonate and diethyl carbonate were dropped on top of the separator.

Electrochemical characterization.—Galvanostatic polarization and relaxation measurements were carried out with a Biologic VMP-300 or VMP-3 potentiostat in a two-electrode setup (ASSB, LEB and TF-LEB cells) which is schematically shown in Fig. 2. The anode was thereby used as a reference electrode, which was lithium metal for the LEB and TF-LEB samples and an In/InLi two-phase alloy for the ASSB samples. The composition of the In/InLi alloy is calculated to be In$_{0.67}$Li$_{0.33}$ or In$_{0.57}$Li$_{0.43}$ in case of fully lithiated or de-lithiated NCM, respectively. Therefore, the composition of the anode for ASSB cells lies well within the two-phase region of In and InLi with a constant potential of around 0.6 V vs Li$^+$/Li.[54] Throughout the study, cells were operated at 25 °C. For the characterization of semi-infinite diffusion, a polarization (charging) current of 4 mA g$_{NCM}^{-1}$ was applied for 2 h followed by a relaxation step for 2 h. After the relaxation step, this polarization/relaxation sequence was continued until the potential of NCM reached approximately 4.3 V vs Li$^+$/Li (3.7 V vs In/InLi). The whole procedure was repeated with a discharge current (4 mA g$_{NCM}^{-1}$) until the potential of NCM reached 2.6 V vs Li$^+$/Li (2.0 V vs In/InLi). For the characterization of finite diffusion, a single charging
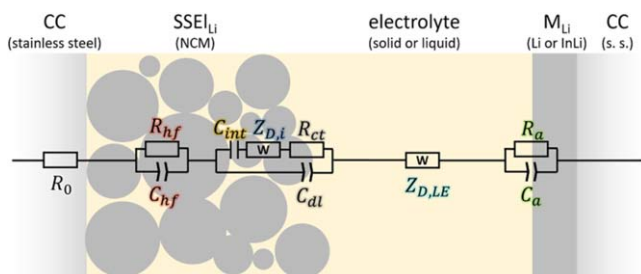

Figure 2. Schematic setup of electrochemical cells and general equivalent circuit for fitting the EIS measurements. The respective impedance elements are color coded so that they can be easily recognized in Fig. 3.

step (4 mA g_{NCM}^{-1}) with various polarization times t_{pol} was performed starting at a potential of around 3.9 V vs Li$^+$/Li, followed by relaxation of V_{OC} for t_{pol} and subsequently followed by a discharging and relaxation step with the same parameters. This measurement was repeated for the TF-LEB cells for different potentials with $t_{pol} = 5$ h.

Following the 2 h relaxation step for the characterization of semi-infinite diffusion by galvanostatic polarization and relaxation, electrochemical impedance spectroscopy (EIS) was performed on LEB and ASSB cells. The measurements were carried out in potentiostatic mode with a Biologic VMP-300 or VMP-3 potentiostat by applying a single sinusoidal input signal with an amplitude of 10 mV superimposed to V_{OC}. The frequency range was 1 MHz to 10 mHz for the ASSB or 1 MHz to 1 mHz for the LEB and TF-LEB, respectively. Galvanostatic or potentiostatic charge and discharge of ASSB and LEB cells was carried out with a MACCOR battery cycler.

Scanning electron microscopy imaging.—LEB and ASSB samples were charged to 4.3 V vs Li$^+$/Li (3.7 V vs In/InLi) and disassembled inside an Ar-filled glovebox afterwards. Recovered cathode composites of LEB samples were rinsed with ethylene carbonate followed by drying overnight in a Büchi oven at 120 °C under vacuum. Control samples were made by disassembling untreated cells. Cross-sectional scanning electron microscopy (SEM) was performed on a XEIA3 FIB-SEM system (Tescan GmbH). Images were taken with an acceleration voltage of 3 kV and emission current of 250 μA and back-scattered electrons were detected.

Results and Discussion

Semi-infinite diffusion and interfacial processes.—Galvanostatic polarization and relaxation measurements were performed on electrochemical half-cells with either liquid electrolyte or solid electrolyte. Exemplary measurements of the relaxation of V_{OC} are shown in Fig. SI-1. The V_{OC} vs time curves were fitted with Eq. 5 to obtain the Warburg coefficient Z_W from which the apparent chemical diffusion coefficient $\tilde{D}_{Li}^{s-i} = \tilde{D}_{Li} \frac{A}{A_0}$ of lithium in NCM was calculated. $\tilde{D}_{Li}^{s-i}$ represents the chemical diffusion coefficient evaluated assuming semi-infinite conditions and corresponds to the actual chemical diffusion coefficient of lithium $\tilde{D}_{Li}$ in NCM not corrected by changes in the electrochemically active surface area A from the nominal surface area A_0. Therefore, any changes during battery cycling that have an effect on the electrochemically surface area, *i. e.* the interface area between electrolyte and NCM, will be reflected in $\tilde{D}_{Li}^{s-i}$. $A_0 = 0.2$ m^2 g^{-1} was measured by Kr-physisorption for the pristine NCM powder. Hereby we note that we assume the NCM to be predominantly an electronic conductor, i. e. the ionic conductivity is by far lower than the electronic conductivity as has been confirmed experimentally.[32]

To obtain more information about the diffusion of lithium, EIS spectra were taken after each relaxation step. Exemplary EIS data are depicted in Figs. 3a and 3b for both the LEB and the ASSB sample, respectively. EIS spectra measured at different potentials are shown in Fig. SI-2. It can be seen that the contribution of the solid electrolyte (R_0 and R_{hf}) to the total impedance is small because of the high conductivity of Li$_6$PS$_5$Cl of >1 mS cm^{-1}.[55] Therefore, we do not expect any significant inhomogeneities of cathode lithiation e.g. due to the reaction zone effect.[29,56] Lithium diffusion inside the NCM phase becomes only dominant, if other processes are fully relaxed. In the ASSB cell this is the case already at frequencies around 0.1 Hz, but for the LEB frequencies below 3 mHz are needed, since the relaxation of the liquid electrolyte occurs with a relaxation time constant of around 40 s. The diffusion impedance with typical values for the liquid electrolyte ($\tilde{D}_{Li}^{LE} \sim 10^{-6}$ cm^2 s^{-1} and $L_{LE} = 130$ μm) fits well to the experimental data, as it is expected to dominate over solid state diffusion in the intermediate frequencies regime.[50,57] Therefore, the first few hundreds of seconds
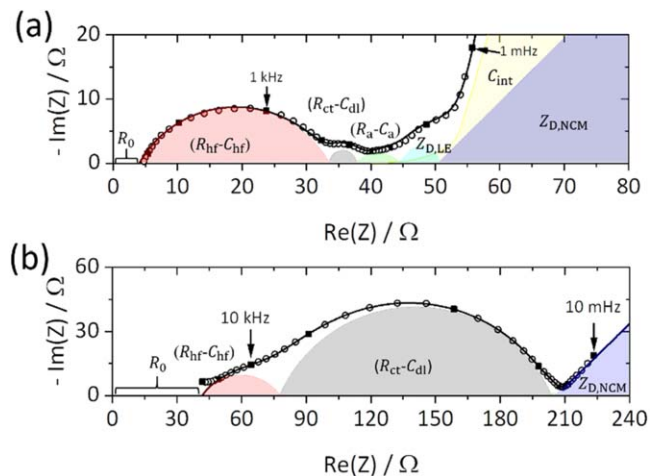

Figure 3. EIS data (circles) of (a) LEB and (b) ASSB cells obtained at around 4 V vs Li$^+$/Li and fitted (lines) with the equivalent circuit shown in Fig. 2. One data point per decade in frequency is shown as a filled square. The respective contributions of the different circuit elements are highlighted for clarity.

of the relaxation of V_{OC} were not included in the fit to assure that exclusively lithium diffusion inside the NCM is investigated. $\tilde{D}_{Li}^{s-i}$ is plotted against the V_{OC} of NCM that was reached after the respective relaxation step. At low frequencies the differential storage capacitance C_{int} adds up to the imaginary part as can be especially seen in the measurement for the LEB, since we chose a lower minimum frequency limit here (1 mHz).

For the calculation of $\tilde{D}_{Li}^{s-i}$ the enhancement factor W is needed, which was obtained from the V_{OC} vs c_{Li} curve according to Eq. 2 (Fig. SI-3), whereas the lithium concentration c_{Li} in NCM was estimated from galvanostatic coulometric titration, assuming faradaic efficiency of 100%. As can be seen, W differs between the measurements by around a factor of 2, which we conclude to be caused by non-faradaic processes that typically occur during the first cycle. Overall, W only differs insignificantly between the LEB and ASSB cells, so it can be concluded that the active material is equally well connected electronically despite carbon was not added to the ASSB cathodes. We note that $\tilde{D}_{Li}^{s-i}$ determined by EIS is in perfect agreement with the data from galvanostatic polarization and relaxation. $\tilde{D}_{Li}^{s-i}$ measured by galvanostatic polarization and relaxation is shown in Fig. 4a) for both the LEB and the ASSB samples, while $\tilde{D}_{Li}^{s-i}$ from EIS measurements is shown in Fig. SI-4 for comparison.

In the beginning of the first charging process $\tilde{D}_{Li}^{s-i}$ is approximately at the same level for the LEB and the ASSB, indicating that the wetting/contacting of the NCM by electrolyte is similar in both cases. Indeed, NCM secondary particles appear to be nearly fully covered by the Li$_6$PS$_5$Cl solid electrolyte (Fig. 5c). We note that carbon and PVDF in the cathode of the LEB may block some of the surface area of the NCM. At low potentials $\tilde{D}_{Li}^{s-i}$ increases steadily for both electrolytes as has been measured for NCM in several reports based on semi-infinite diffusion. It has been shown by first-principles simulations that such an increase can be explained by the formation of lithium ion vacancies that enables the transport of Li$^+$ via a divacancy-hopping mechanism that is much faster than the hopping through the oxygen dumbbell that occurs in highly lithiated NCM at low potentials.[58,59] Also, recent studies by NMR spectroscopy suggest fast lithium diffusion at intermediate lithiation and slow diffusion at the high- and low-potential limits.[60]

At around 3.7 V vs Li$^+$/Li and continuing, $\tilde{D}_{Li}^{s-i}$ saturates for the ASSB. However, at around 3.8 V vs Li$^+$/Li, $\tilde{D}_{Li}^{s-i}$ shows a further strong increase for the LEB, whereas it remains at a constant level for the ASSB. This discrepancy cannot be explained by the lithium transport mechanism itself, and thus, is related to morphological changes that affect the electrochemically active interface area A. The
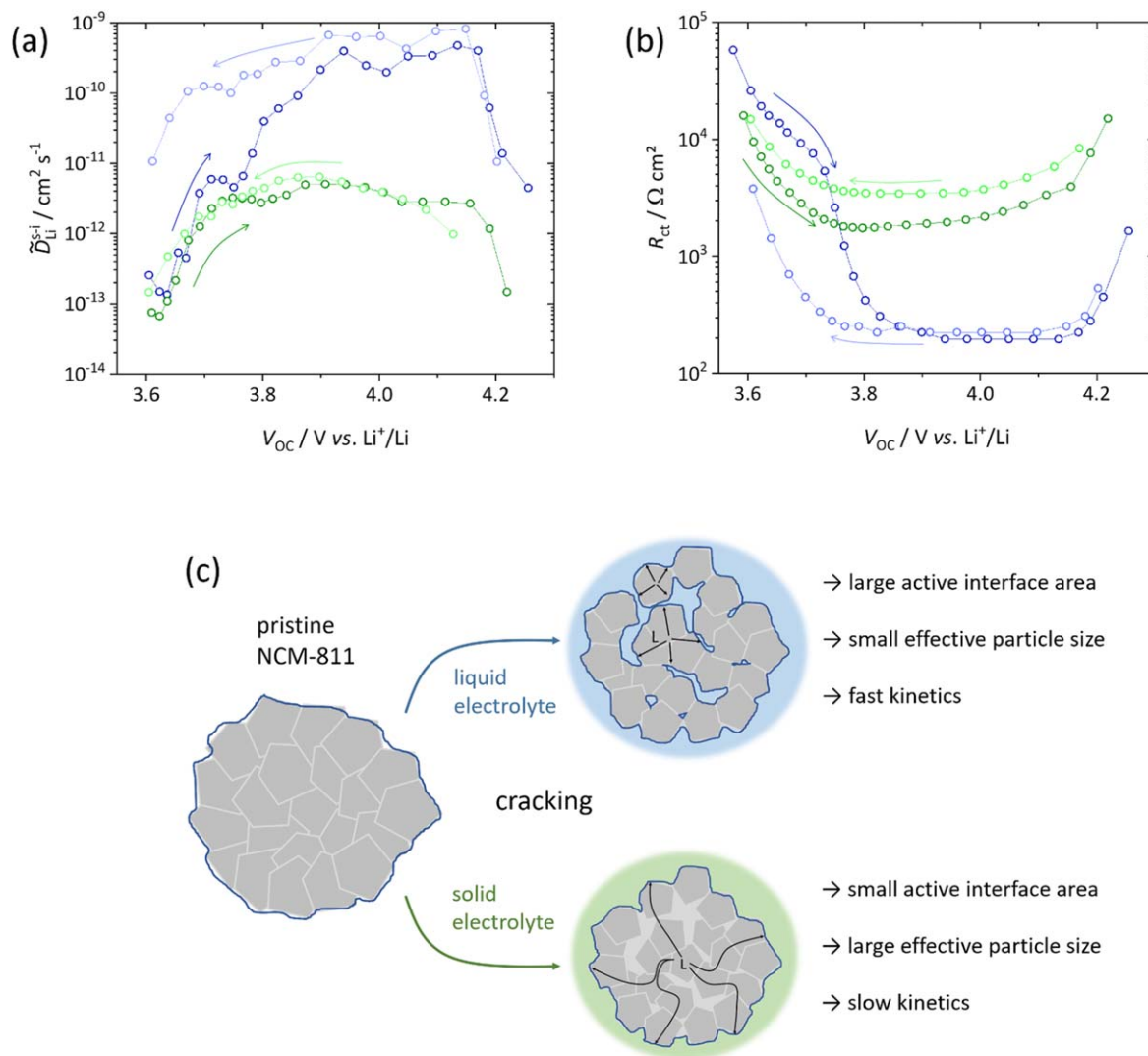
Figure 4. (a) The apparent diffusion coefficient $\tilde{D}_{Li}^{s-i}$ experimentally determined from galvanostatic polarization and relaxation measurements and (b) R_{ct} from EIS measurements for LEB (blue) and ASSB (green) samples obtained during the first charge (dark colors) and the following discharge (light colors). (c) Schematic illustration of the effect of cracking of secondary particles of NCM on the effective particle size and electrochemically active surface area when in contact to a liquid or solid electrolyte.

commonly employed NCM-based electrodes consist of μm-sized secondary particles that themselves consist of randomly oriented primary particles with sizes of a few hundreds of nanometers (Fig. 5a). The observation of micro- and/or nanocrack formation in secondary particles of NCM has frequently been reported.[61–67] While pristine NCM secondary particles are densely packed, they show cracks along the primary particle boundaries already after the first cycle charge (Figs. 5b and 5c). These cracks can be observed at the secondary particle's surface and eventually penetrate the full particle volume and can be infiltrated by the liquid electrolyte leading to a microstructural degradation of the material.[25,61,66] We note, that especially cracks with sizes of few nanometers can be penetrated by the liquid electrolyte but are hardly resolved by SEM. It also appears from the SEM images that cracking of NCM is more prominent in the LEB as compared to the ASSB cathodes. Although the high bulk modulus of NCM prevents any significant compression during charging and, thus, any effect on the anisotropic strain development in the NCM,[20] certain coatings are observed to prevent serious cracking.[68] This may suggest that also the solid electrolyte can have an effect on cracking but a more sophisticated study is needed to confirm this hypothesis. The results can also be influenced by other factors such as the higher overpotentials during charging of

the ASSB. Nonetheless, NCM is reported to suffer cracking also in ASSB cells with Li_6PS_5Cl solid electrolyte such as presently used, and we cannot exclude statistical effects.[69]

Interestingly, during the first charge starting at around 3.8 V vs Li^+/Li and continuing until the upper cutoff potential is reached, acoustic signals evolve from $LiNiO_2$ electrodes that can be attributed to plastic deformation and cracking.[70] Cracks in the secondary particles of NCM increase the surface area for the liquid electrolyte, but not for the solid electrolyte as illustrated in Fig. 4c). As a consequence, the semi-infinite diffusion kinetics is by orders of magnitude faster for the LEB than for the ASSB. Furthermore, Oswald et al. found an increase in the double-layer capacitance at the $LiNi_{0.6}Co_{0.2}Mn_{0.2}O_2$ | electrolyte interface indicating an increased surface area because of cracking, even when the battery was only cycled up to 3.9 V vs Li^+/Li.[71] At high potentials a drop of $\tilde{D}_{Li}^{s-i}$ is observed for both the LEB and ASSB. This is most likely related to the shrinking interlayer spacing between the TM-O_2 slabs (TM = transition metal). The interlayer spacing collapses drastically at low degrees of lithiation, especially in high-Ni NCM materials such as presently used.[64,72,73]

The measurement of $\tilde{D}_{Li}^{s-i}$ during discharge reversibly follows the measurement during charge for the ASSB. This further corroborates
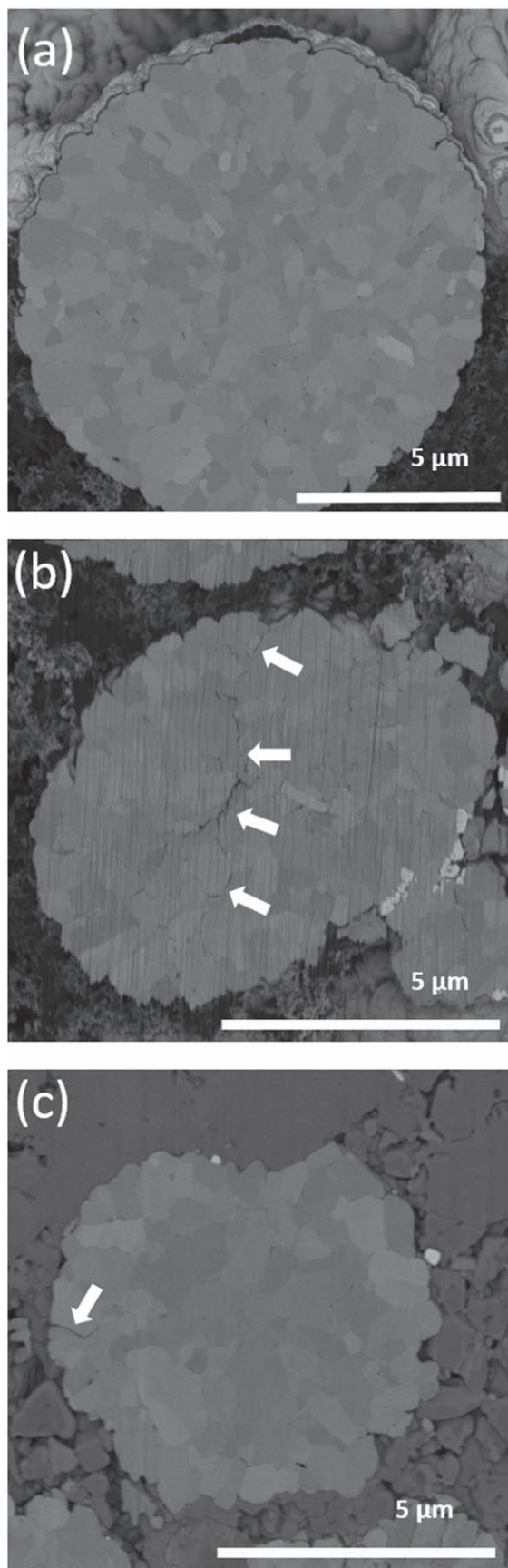
Figure 5. Cross-sectional SEM images of (a) a pristine NCM secondary particle and an NCM particle after the first cycle charging step in a (b) LEB or (c) ASSB cathode composite. Arrows highlight cracks inside the secondary particles.

that the morphological evolution of the cathode has basically no effect on the diffusion kinetics of the ASSB and the contact-loss induced by volume contraction of the NCM is minimal at least during the first cycle. This is in contrast to a significant discrepancy between $\tilde{D}_{Li}^{s\text{-}i}$ measured during charge and discharge found for the LEB, which is explained by the fact, that the cracks in the secondary particles typically remain in the material even during re-lithiation.[70] Similar observations have also been made in earlier studies that explicitly measure $\tilde{D}_{Li}^{s\text{-}i}$ during the first charge-discharge cycle.[74] Consequently, a higher electrochemically active surface area remains in the LEB leading to significantly faster lithium insertion/extraction kinetics than in the ASSB, also in the following charge/discharge cycles. The effects of this phenomenon on the battery performance are discussed in detail below. We also note that cells are often treated by several charge-discharge cycles before the diffusion coefficient is measured by similar techniques. This can lead to incorrect values if the actual surface area after cracking is not properly taken into account.

In correspondence to $\tilde{D}_{Li}^{s\text{-}i}$, the interfacial charge-transfer resistance at the NCM | electrolyte interface R_{ct} (Fig. 4b) shows different behavior for the LEB and ASSB cells. A steep decrease of R_{ct} is observed for the LEB between 3.7–3.8 V vs Li$^+$/Li, corresponding to the sharp increase of $\tilde{D}_{Li}^{s\text{-}i}$. Also the discrepancy between the measurements during charge and discharge is present as observed earlier for $\tilde{D}_{Li}^{s\text{-}i}$. Similarly, Chiang et al. observed a reduction of the charge-transfer resistance by one order of magnitude when comparing the measurement during discharge with the measurement during charge on single LiNi$_{0.33}$Co$_{0.33}$Mn$_{0.33}$O$_2$ secondary particles.[74] Furthermore, the expected parabolic shape of R_{ct}, resulting from its dependence on the lithium ion concentration at the NCM|electrolyte interface, can clearly be observed with a minimum at around Li$_{0.5}$Ni$_{0.8}$Co$_{0.1}$Mn$_{0.1}$O$_2$, corresponding to around 3.9 V vs Li$^+$/Li.[25,49,74,75] Other than $\tilde{D}_{Li}^{s\text{-}i}$, R_{ct} shows significantly higher values for the ASSB during discharge than during charge. This was already subject of past studies and is a consequence of irreversible reactions at the CAM | electrolyte interface.[10,15,76] However, since $\tilde{D}_{Li}^{s\text{-}i}$ clearly does not show such difference between charge and discharge, we conclude that the irreversible reaction is not related to contact loss, but is rather caused by the formation of a high-impedance insulating layer at the interface.[52]

Finite diffusion—diffusion at long polarization times.— Galvanostatic polarization and relaxation measurements were performed with a charging current, subsequently followed by a measurement with a discharging current. According to Eq. 9 this procedure allows the reliable determination of the diffusion-related relaxation at long relaxation times. By fitting the V_{OC} vs time curves as described in the previous section, the apparent relaxation time τ_{app} was extracted. A series of measurements were taken for various values of the polarization time t_{pol}. Exemplary measurements are shown in Fig. SI-6. τ_{app} vs t_{pol} is depicted in Fig. 6a, clearly showing a correlation. This is due to the intriguing fact that only semi-infinite diffusion is observed for short t_{pol}, where $\tau_{app} \approx 4t_{pol}$ holds and thus τ_{app} does not contain any direct information on the finite diffusion of lithium.

For the ASSB, τ_{app} follows the predicted trend $\tau_{app} = 4t_{pol}$ and seems to significantly deviate only for $t_{pol} > 50$ h, giving a lower boundary for the real relaxation time $\tau > 200$ h. As discussed in the methods section, the condition $\tau_{app} = 4t_{pol}$ is a consequence of Eqs. 5 and 6 and, if fulfilled, implies that diffusion in NCM has to be considered as semi-infinite under the given conditions. At $t_{pol} = 50$ h, finite diffusion is achieved only in the smaller sized particles of NCM, but τ still keeps increasing with t_{pol}, because the diffusion in the larger sized particles is still semi-infinite. Therefore, this also defines an upper boundary for the chemical diffusion coefficient $\tilde{D}_{Li}^{f} < 10^{-13}$ cm^2 s^{-1}, if an average particle radius of 3 μm (Fig. SI-5) is considered as the diffusion layer thickness. $\tilde{D}_{Li}^{f}$ is

the chemical diffusion coefficient evaluated assuming finite conditions and does not depend on other parameters, rather only on the length of the pathway for lithium diffusion. However, the diffusion pathway needs to cross primary particle boundaries and can eventually become tortuous due to particle cracking (Fig. 5), which would explain the lower value of $\tilde{D}_{Li}^{f}$ as compared to $\tilde{D}_{Li}^{s-i}$, especially for the ASSB. A schematic representation of the influence of different diffusion pathways on the measured values of $\tilde{D}_{Li}^{f}$ and $\tilde{D}_{Li}^{s-i}$ is provided in Scheme 1.

For the LEB, we observe that τ_{app} deviates for small t_{pol} from the trend predicted for exclusively semi-infinite diffusion. This can be attributed to a lower effective particle size caused by cracking and, thus, shorter effective lithium diffusion pathways in accordance to the observation that the liquid electrolyte penetrates the cracks in the secondary particle of NCM (as illustrated in Fig. 4c). This shows that finite diffusion is established much earlier in LEB cells than in ASSB cells, highlighting that full utilization of active material in the LEB can be achieved at much higher rates. However, no clear saturation of τ_{app} vs t_{pol} is observed, which we expect at sufficiently high t_{pol}. We believe that the effective particle size becomes rather undefined in this case, leading to a broad distribution of effective lithium diffusion pathways. Consequently, $\tilde{D}_{Li}^{f}$ cannot be reliably determined in this case.

To address this issue, we prepared a thin film of $LiNi_{0.33}Co_{0.33}Mn_{0.33}O_2$ as one-dimensional diffusion model system and employed it as cathode in a liquid electrolyte half-cell (TF-LEB). On the one hand thin film electrodes have a well-defined and uniform thickness and on the other hand NCM-333 is less prone to severe volume changes, leading to less fracture.[64] As seen in Fig. 6a for the TF-LEB, τ_{app} follows the trend predicted for semi-infinite diffusion at short t_{pol}. From $t_{pol} \approx 2$ h, τ_{app} reaches a constant value of $\tau_{app} = \tau \approx 8$ h, corresponding to $\tilde{D}_{Li}^{f} \approx 4 \cdot 10^{-14}$ cm^2 s^{-1} at around 3.9 V vs Li$^+$/Li. It has to be taken into account that the thin film electrode is chemically and morphologically different from the particulate NCM and, thus, different values for $\tilde{D}_{Li}^{f}$ are expected. We note that the presently employed NCM thin film shows no preferential orientation as can be seen in the X-ray diffraction pattern (Fig. SI-7). Overall, this demonstrates the slow diffusion of lithium into NCM and highlights the significant differences between semi-infinite and finite diffusion kinetics.

A series of such experiments were performed with the TF-LEB at different potentials and with a constant $t_{pol} = 5$ h and the resulting $\tilde{D}_{Li}^{f}$ is shown in Fig. 6b. It is important to note that this t_{pol} only allows a reliable measurement for $\tilde{D}_{Li}^{f} > 10^{-14}$ cm^2 s^{-1}. $\tilde{D}_{Li}^{f}$ shows a local minimum at around 3.75 V vs Li$^+$/Li as also predicted by Wei et al. from first-principles calculations.[58] In Fig. 6b, also the enhancement factor W is shown, which has been determined as described in the previous section. W links $\tilde{D}_{Li}^{f}$ with the self or lattice diffusion coefficient D_{Li}^{f} via $\tilde{D}_{Li}^{f} = W \, D_{Li}^{f}$.[43] Accordingly, D_{Li}^{f} was calculated from $\tilde{D}_{Li}^{f}$ and appears to be constant for potentials >3.7 V vs Li$^+$/Li, showing a drop for potentials <3.7 V vs Li$^+$/Li. A widely

constant D_{Li}^{f} was also observed by Jang et al. for LiCoO$_2$ in a corresponding range of lithiation.[38] This shows that the chemical diffusion in this range is dominated by the electrostatic repulsion between the inserted lithium ions, while the drop of both D_{Li}^{f} and $\tilde{D}_{Li}^{f}$ at high degree of lithiation (low potential) might be associated to the
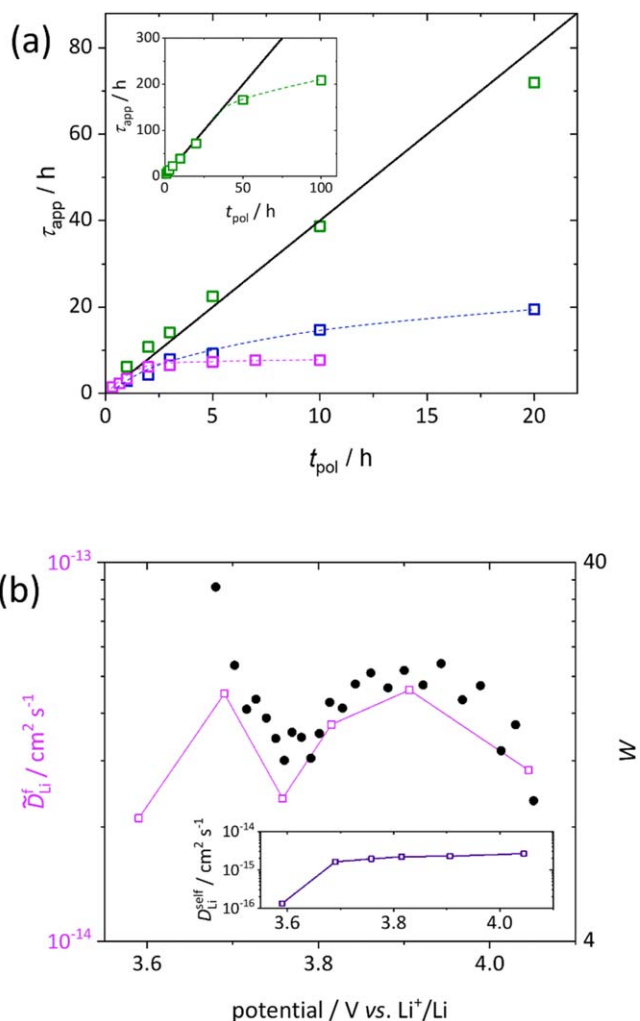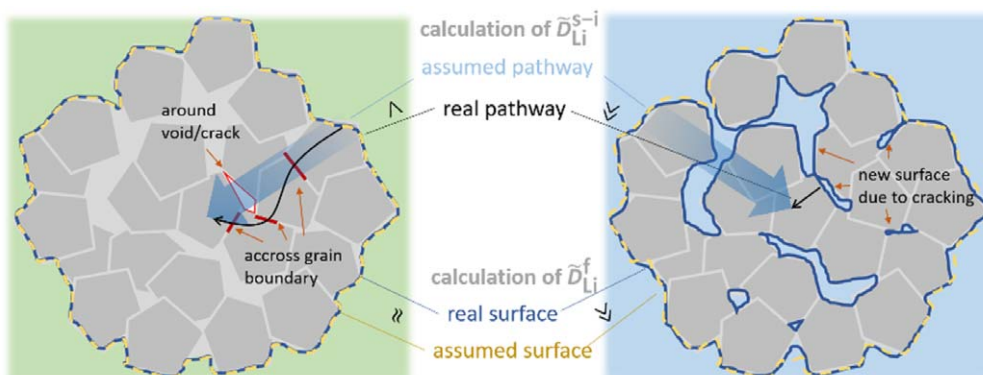
Figure 6. (a) Relationship between τ_{app} and t_{pol} for ASSB (green), LEB (blue) and TF-LEB (purple) and the prediction relation $\tau_{app} = 4t_{pol}$ in case of semi-infinite diffusion only (straight line) from Eqs. 5 and 6. Dashed lines are provided as a guide to the eye. The inset shows the measurements for the ASSB at longer t_{pol}. (b) $\tilde{D}_{Li}^{f}$ (purple), W (black) and D_{Li}^{f} (inset) for a TF-LEB sample measured with $t_{pol} = 5$ h.

Scheme 1. Illustration of diffusion pathways and surface areas relevant for the calculation of $\tilde{D}_{Li}^{f}$ and $\tilde{D}_{Li}^{s-i}$ of NCM in the ASSB cell (left) and the LEB cell (right).

change in the transport mechanism between oxygen dumbbell hopping (ODH) and tetrahedral site hopping (TSH).[58] W, $\tilde{D}_{Li}^{f}$ (Fig. 6b) and $\tilde{D}_{Li}^{s-i}$ (Fig. 4a) reach a peak value at around 3.9 V vs Li$^+$/Li which corresponds to Li$_{0.5}$Ni$_{0.8}$Co$_{0.1}$Mn$_{0.1}$O$_2$, where a maximum was found also for Li$_{0.5}$CoO$_2$ that results from order/disorder transitions.[38]

Implications of diffusion kinetics on battery performance.— From the results of the semi-infinite and finite lithium diffusion inside NCM, it can be concluded that the kinetics in the LEB are significantly faster than in the ASSB as a consequence of the ability of the liquid electrolyte to infiltrate evolving micro- and nanocracks in the secondary particles of NCM. Beyond that, it is of interest to elucidate the impact of this phenomenon on the battery performance. In Fig. 7 typical charge-discharge characteristics of LEB (blue) and ASSB (green) half-cells are shown for a galvanostatic charge and discharge with 20 mA g$_{NCM}$$^{-1}$ in a voltage range between 2.6–4.3 V vs Li$^+$/Li. It can clearly be seen that the LEB not only shows higher overall specific capacities after the first charge (207 mAh g$_{NCM}$$^{-1}$ (LEB) vs 186 mAh g$_{NCM}$$^{-1}$ (ASSB)), but also a higher Coulombic efficiency in the first charge-discharge cycle (85% (LEB) vs 72% (ASSB)) as well as a better capacity retention. However, capacity fading is quite notably for both the LEB and the ASSB cells even in the first cycles as shown in the inset of Fig. 7. In both cases, the chemo-mechanical evolution of NCM is believed to play a major role in the long-term cycling performance.[10,63,64] Nonetheless, different effects of chemo-mechanics, i.e. cracking, on the capacity retention of LEB and ASSB cells are expected, but the investigation of this is beyond the scope of this paper. As demonstrated by Kasnatscheew et al. the main part of the first-cycle capacity-loss in NCM-based cells is due to kinetic limitations during discharge, even in cells with liquid electrolyte.[24] Therefore, we will focus on the first-cycle capacity-loss in the following.

It is worth to note that Fig. 7 reveals generally higher overpotentials in the ASSB caused by higher internal resistances. However, during the first charge the difference in overpotentials between LEB and ASSB seems to become more significant at around 3.8 V vs Li$^+$/Li, corroborating the findings shown in Figs. 4a and 4b. The high overpotentials in the ASSB also lead to the missing plateau at around 4.2 V vs Li$^+$/Li, which is only present for the LEB.

To quantify the capacity-loss due to slow kinetics, we performed a potentiostatic step at the lower cutoff potential (2.6 V vs Li$^+$/Li) for 24 h at the end of the galvanostatic discharge of LEB and ASSB
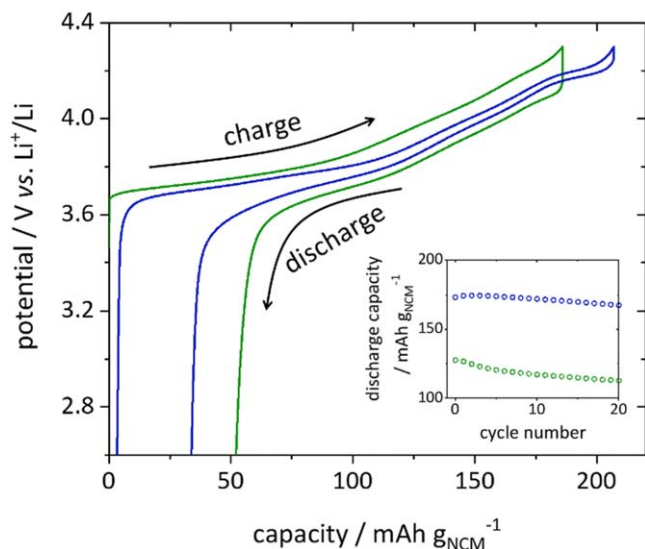
cells. The extracted current was recorded over time and is shown in Fig. 8a). The experiment was repeated for various galvanostatic discharge currents. It can be seen that the re-lithiation of NCM occurs significantly faster in the LEB than in the ASSB. Obviously, this can be attributed to the faster kinetics in the LEB as a consequence of the higher electrochemical surface area and lower effective particle size as discussed in the previous sections. Comparable observations were made by Strauss et al. when comparing NCM-electrodes made with either small, medium-sized or large secondary particles.[77] While the initial secondary particle size had no effect on the first-cycle capacity-loss on LEBs, the Coulombic efficiency of ASSBs dropped from 70% (small particles) to only 50% (large particles).[77] Based on our results we conclude that the initial particles size has no fundamental influence on the kinetics in LEBs, since cracking determines the effective particle size and surface area, other than for ASSBs, where the initial particle size is decisive.
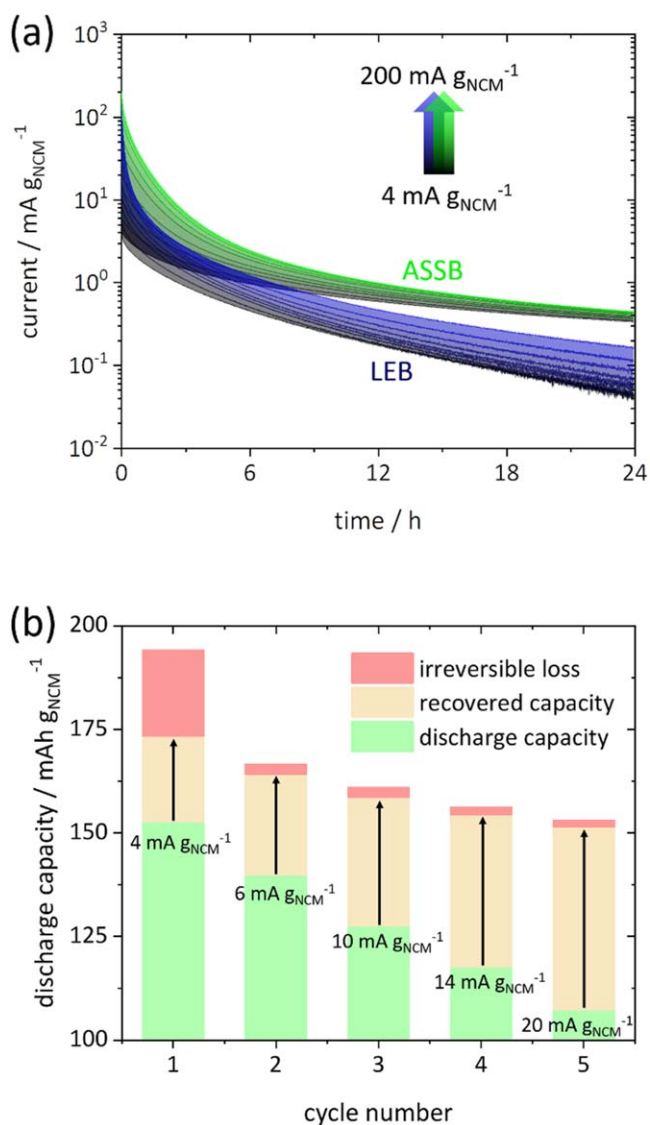
Figure 8. (a) Potentiostatic discharge at 2.6 V vs Li$^+$/Li following galvanostatic discharge at various currents for LEB (blue) and ASSB (green) samples. The charging current was kept constant at 4 mA g$_{NCM}$$^{-1}$. (b) Charge and discharge capacities for the ASSB sample shown in (a). The capacity recovered during the potentiostatic discharge is shown as a black arrow and the galvanostatic discharge current is indicated. The irreversible capacity loss is the difference between the charge capacity and total (sum of galvanostatic and potentiostatic) discharge capacity.

Figure 7. First-cycle galvanostatic charge and discharge profiles with 20 mA g$_{NCM}$$^{-1}$ in the range between 2.6–4.3 V vs Li$^+$/Li for a LEB (blue) and a ASSB (green) The corresponding specific discharge capacity for the first 20 cycles is shown in the inset.
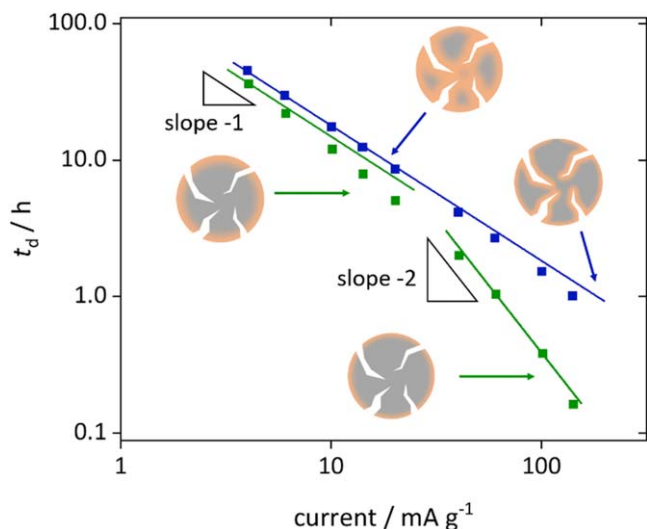
Figure 9. Double-logarithmic plot of the discharge time t_d and the galvanostatic discharge current for LEB (blue) and ASSB (green) samples. Regimes of finite or semi-infinite diffusion control are indicated.

To underline the drastic importance of such kinetic limitation for the ASSB performance, the recovered capacities after the galvanostatic discharge with various currents are shown in Fig. 8b). Even after a very slow discharge with 4 mA g_{NCM}^{-1} about half of the capacity-loss during the first cycle can be recovered (reversible capacity-loss) leading to an overall discharge capacity of 173 mAh g_{NCM}^{-1} and a Coulombic efficiency of 89%. In addition, we note that the current during the potentiostatic step only reached around 10% of its initial value after 24 h and, therefore, even more capacity should be recoverable. The resulting irreversible capacity-loss of <20 mAh g_{NCM}^{-1} can be attributed to parasitic reactions, such as the self-limiting formation of a solid-electrolyte interphase (SEI). Although the electrochemical stability window of the presently used Li_6PS_5Cl solid electrolyte is by far exceeded at the NCM | electrolyte interface,[55] the irreversible capacity-loss appears rather mild and proves the practical applicability of such materials for ASSBs, if the kinetic limitations are overcome. At higher discharge current, the reversible capacity-loss increases drastically, further highlighting the detrimental effect of kinetic limitations on the rate capability of ASSBs. We note that the stability window is also exceeded at the In/InLi | electrolyte interface.[55] However, we do not see any significant impedance contribution throughout the whole experiment (Fig. 3b) and Figs. SI-2c and SI-2d), which would be expected at around 1 Hz.[51]

In Fig. 9, the discharge time t_d vs the discharge current is shown in a double logarithmic plot. t_d is the time the cell can be galvanostatically discharged at a certain current from the fully charged state until the lower cutoff potential is reached. From basic considerations a slope of −1 would be expected for finite and a slope of −2 for solely semi-infinite diffusion during the discharge.[29] It can be seen that for moderate t_d only the LEB clearly shows finite diffusion during discharge while even at very long t_d this cannot be clearly stated for the ASSB, as also expected from Fig. 6a. This emphasizes that the full volume of the NCM particles cannot be utilized in the ASSB during battery cycling and can be considered inactive, contributing negatively to the gravimetric capacity. The differences between the ASSB and the LEB especially come into play at higher discharge currents. For shorter t_d, solely semi-infinite diffusion is observed for the ASSB and at very short t_d the slope is becoming smaller than −2 indicating a tendency towards charge-transfer limitation rather than diffusion limitation. To address the issue of the low rate capability of ASSBs, an increase of the NCM | solid electrolyte interface area and a shortening of pathways for lithium diffusion appears to be necessary. Another alternative is to create secondary particles of NCM with oriented primary particles to assist transport into the particle volume.[69,78]

Conclusions

Chemical diffusion coefficients of lithium in $LiNi_{0.8}Co_{0.1}Mn_{0.1}O_2$ (NCM) electrodes were measured by techniques utilizing semi-infinite or finite diffusion for battery half-cells using either liquid or solid electrolytes. For cells with liquid electrolyte, evolving cracks in the NCM can be infiltrated by the electrolyte, leading to significant increases in the electrochemically active interface area that result in a higher apparent diffusion coefficient, a shortening of pathways for lithium diffusion and also improved charge-transfer kinetics at the liquid electrolyte | NCM interface. In total, the faster kinetics is found to be essential for the superior performance of liquid electrolyte-based cells compared to solid electrolyte-based cells. Solid electrolytes lack the ability to benefit from the cracking of NCM particles and the slower kinetics lead to drastic losses in capacity, shown to be crucial even at low cycling rates. However, the chemical diffusion coefficients determined in solid electrolyte cells appear more reliable than in liquid electrolyte cells as they are not vastly overestimated by the increase of NCM surface area during measurement.

By accounting for the slow kinetics with a constant potential step at the end of the galvanostatic discharge step, we show that a Coulombic efficiency of more than 89% and a discharge capacity of more than 173 mAh g_{NCM}^{-1} can be achieved for the first charge-discharge cycle in all-solid state battery half-cells. Based on these results, a pathway for further improvements on overall capacity and rate capability of all-solid state batteries is discussed.

ORCID

Raffael Ruess ⓘ https://orcid.org/0000-0002-9274-4714
Simon Schweidler ⓘ https://orcid.org/0000-0003-4675-1072
Hendrik Hemmelmann ⓘ https://orcid.org/0000-0003-1349-3054
Gioele Conforto ⓘ https://orcid.org/0000-0003-4922-6679
Anja Bielefeld ⓘ https://orcid.org/0000-0003-2193-8375
Dominik A. Weber ⓘ https://orcid.org/0000-0003-4357-9713
Joachim Sann ⓘ https://orcid.org/0000-0003-4663-2671
Matthias T. Elm ⓘ https://orcid.org/0000-0001-7014-5772
Jürgen Janek ⓘ https://orcid.org/0000-0002-9221-4756

References

1. D. Larcher and J.-M. Tarascon, *Nat. Chem.*, **7**, 19 (2015).
2. S. Chu and A. Majumdar, *Nature*, **488**, 294 (2012).
3. L. Lu, X. Han, J. Li, J. Hua, and M. Ouyang, *J. Power Sources*, **226**, 272 (2013).
4. J. Janek and W. G. Zeier, *Nat. Energy*, **1**, 1167 (2016).
5. A. Manthiram, J. C. Knight, S.-T. Myung, S.-M. Oh, and Y.-K. Sun, *Adv. Energy Mater.*, **6**, 1501010 (2016).
6. S.-T. Myung, F. Maglia, K.-J. Park, C. S. Yoon, P. Lamp, S.-J. Kim, and Y.-K. Sun, *ACS Energy Lett.*, **2**, 196 (2017).
7. L. de Biasi, A. O. Kondrakov, H. Geßwein, T. Brezesinski, P. Hartmann, and J. Janek, *J. Phys. Chem. C*, **121**, 26163 (2017).
8. J. E. Harlow et al., *J. Electrochem. Soc.*, **166**, A3031 (2019).
9. J. Kasnatscheew, M. Evertz, B. Streipert, R. Wagner, S. Nowak, I. Cekic Laskovic, and M. Winter, *J. Power Sources*, **359**, 458 (2017).
10. R. Koerver, I. Aygün, T. Leichtweiß, C. Dietrich, W. Zhang, J. O. Binder, P. Hartmann, W. G. Zeier, and J. Janek, *Chem. Mater.*, **29**, 5574 (2017).
11. J. Auvergniot, A. Cassel, J.-B. Ledeuil, V. Viallet, V. Seznec, and R. Dedryvère, *Chem. Mater.*, **29**, 3883 (2017).
12. H. Lee, P. Oh, J. Kim, H. Cha, S. Chae, S. Lee, and J. Cho, *Adv. Mater.*, **31**, e1900376 (2019).

13. W. Zhang, T. Leichtweiß, S. P. Culver, R. Koerver, D. Das, D. A. Weber, W. G. Zeier, and J. Janek, *ACS Appl. Mater. Inter.*, **9**, 35888 (2017).
14. Y. Kato, S. Hori, T. Saito, K. Suzuki, M. Hirayama, A. Mitsui, M. Yonemura, H. Iba, and R. Kanno, *Nat. Energy*, **1**, 652 (2016).
15. S.-K. Jung, H. Gwon, S.-S. Lee, H. Kim, J. C. Lee, J. G. Chung, S. Y. Park, Y. Aihara, and D. Im, *J. Mater. Chem. A*, **7**, 22967 (2019).
16. T. Yoshinari, R. Koerver, P. Hofmann, Y. Uchimoto, W. G. Zeier, and J. Janek, *ACS Appl. Mater. Inter.*, **11**, 23244 (2019).
17. A.-Y. Kim, F. Strauss, T. Bartsch, J. H. Teo, T. Hatsukade, A. Mazilkin, J. Janek, P. Hartmann, and T. Brezesinski, *Chem. Mater.*, **31**, 9664 (2019).
18. S. P. Culver, R. Koerver, W. G. Zeier, and J. Janek, *Adv. Energy Mater.*, **9**, 1900626 (2019).
19. K. Takada, N. Ohta, L. Zhang, K. Fukuda, I. Sakaguchi, R. Ma, M. Osada, and T. Sasaki, *Solid State Ionics*, **179**, 1333 (2008).
20. R. Koerver, W. Zhang, L. de Biasi, S. Schweidler, A. O. Kondrakov, S. Kolling, T. Brezesinski, P. Hartmann, W. G. Zeier, and J. Janek, *Energy Environ. Sci.*, **11**, 2142 (2018).
21. P. Wang, W. Qu, W.-L. Song, H. Chen, R. Chen, and D. Fang, *Adv. Funct. Mater.*, **500**, 1900950 (2019).
22. A. Bielefeld, D. A. Weber, and J. Janek, *J. Phys. Chem. C*, **123**, 1626 (2019).
23. T. Liu, Y. Zhang, R. Chen, S.-X. Zhao, Y. Lin, C.-W. Nan, and Y. Shen, *Electrochem. Commun.*, **79**, 1 (2017).
24. J. Kasnatscheew et al., *Phys. Chem. Chem. Phys.*, **18**, 3956 (2016).
25. F. Friedrich, B. Strehle, A. T. S. Freiberg, K. Kleiner, S. J. Day, C. Erk, M. Piana, and H. A. Gasteiger, *J. Electrochem. Soc.*, **166**, A3760 (2019).
26. S.-H. Kang, W.-S. Yoon, K.-W. Nam, X.-Q. Yang, and D. P. Abraham, *J. Mater. Sci.*, **43**, 4701 (2008).
27. H. Zhou, F. Xin, B. Pei, and M. S. Whittingham, *ACS Energy Lett.*, **4**, 1902 (2019).
28. W. Zhang et al., *ACS Appl. Mater. Inter.*, **9**, 17835 (2017).
29. M. Doyle and J. Newman, *J. Appl. Electrochem.*, **27**, 846 (1997).
30. R. E. Usiskin and J. Maier, *Phys. Chem. Chem. Phys.*, **20**, 16449 (2018).
31. M.-C. Pang, Y. Hao, M. Marinescu, H. Wang, M. Chen, and G. J. Offer, *Phys. Chem. Chem. Phys.*, **21**, 22740 (2019).
32. R. Amin and Y.-M. Chiang, *J. Electrochem. Soc.*, **163**, A1512 (2016).
33. X. H. Rui, N. Ding, J. Liu, C. Li, and C. H. Chen, *Electrochim. Acta*, **55**, 2384 (2010).
34. Y. Zhu and C. Wang, *J. Phys. Chem. C*, **114**, 2830 (2010).
35. S. Burkhardt, M. T. Elm, B. Lani-Wayda, and P. J. Klar, *Adv. Mater. Interfaces*, **5**, 1701587 (2018).
36. I. O. Santos-Mendoza, J. Vázquez-Arenas, I. González, G. Ramos-Sánchez, and C. O. Castillo-Araiza, *Int. J. Chem. React. Eng.*, **17**, 20180095 (2019).
37. Z. Shen, L. Cao, C. D. Rahn, and C.-Y. Wang, *J. Electrochem. Soc.*, **160**, A1842 (2013).
38. Y.-I. Jang, B. J. Neudecker, and N. J. Dudney, *Electrochem. Solid-State Lett.*, **4**, A74 (2001).
39. J. Li, F. Yang, X. Xiao, M. W. Verbrugge, and Y.-T. Cheng, *Electrochim. Acta*, **75**, 56 (2012).
40. M. D. Levi and D. Aurbach, *Electrochim. Acta*, **45**, 167 (1999).
41. A. Honders, J. Derkinderen, A. van Heeren, J. de Wit, and G. Broers, *Solid State Ionics*, **15**, 265 (1985).
42. W. Weppner and R. A. Huggins, *J. Electrochem. Soc.*, **124**, 1569 (1977).
43. C. J. Wen, B. A. Boukamp, R. A. Huggins, and W. Weppner, *J. Electrochem. Soc.*, **126**, 2258 (1979).
44. M. D. Levi, G. Salitra, B. Markovsky, H. Teller, D. Aurbach, and U. Heider, *J. Electrochem. Soc.*, **146**, 1279 (1999).
45. S. Cui et al., *Adv. Energy Mater.*, **6**, 1501309 (2016).
46. C. Ho, I. D. Raistrick, and R. A. Huggins, *J. Electrochem. Soc.*, **127**, 343 (1980).
47. G. Pistoia, A. Antonini, R. Rosati, and D. Zane, *Electrochim. Acta*, **41**, 2683 (1996).
48. M. D. Levi and D. Aurbach, *J. Phys. Chem. B*, **101**, 4630 (1997).
49. M. Schönleber, C. Uhlmann, P. Braun, A. Weber, and E. Ivers-Tiffée, *Electrochim. Acta*, **243**, 250 (2017).
50. J. Landesfeind, D. Pritzl, and H. A. Gasteiger, *J. Electrochem. Soc.*, **164**, A1773 (2017).
51. A. Sakuda, H. Kitaura, A. Hayashi, K. Tadanaga, and M. Tatsumisago, *J. Electrochem. Soc*, **156**, A27 (2009).
52. F. Walther, S. Randau, Y. Schneider, J. Sann, M. Rohnke, F. H. Richter, W. G. Zeier, and J. Janek, *Chem. Mater.* (2020).
53. H. Hemmelmann, J. K. Dinter, and M. T. Elm, *ACS Appl. Energy Mater.* (2020).
54. A. L. Santhosha, L. Medenbach, J. R. Buchheim, and P. Adelhelm, *Batteries & Supercaps*, **2**, 524 (2019).
55. G. F. Dewald, S. Ohno, M. A. Kraft, R. Koerver, P. Till, N. M. Vargas-Barbosa, J. Janek, and W. G. Zeier, *Chem. Mater.*, **31**, 8328 (2019).
56. Y. Kato, S. Shiotani, K. Morita, K. Suzuki, M. Hirayama, and R. Kanno, *J. Phys. Chem. Lett.*, **9**, 607 (2018).
57. X. Zhou, J. Huang, Z. Pan, and M. Ouyang, *J. Power Sources*, **426**, 216 (2019).
58. Y. Wei et al., *J. Am. Chem. Soc.*, **137**, 8364 (2015).
59. A. van der Ven and G. Ceder, *J. Power Sources*, **97–98**, 529 (2001).
60. K. Märker, P. J. Reeves, C. Xu, K. J. Griffith, and C. P. Grey, *Chem. Mater.*, **31**, 2545 (2019).
61. H.-H. Ryu, K.-J. Park, C. S. Yoon, and Y.-K. Sun, *Chem. Mater.*, **30**, 1155 (2018).
62. J.-M. Lim, T. Hwang, D. Kim, M.-S. Park, K. Cho, and M. Cho, *Sci. Rep.*, **7**, 39669 (2017).
63. S. Schweidler, L. de Biasi, G. Garcia, A. Mazilkin, P. Hartmann, T. Brezesinski, and J. Janek, *ACS Appl. Energy Mater.*, **2**, 7375 (2019).
64. A. O. Kondrakov, A. Schmidt, J. Xu, H. Geßwein, R. Mönig, P. Hartmann, H. Sommer, T. Brezesinski, and J. Janek, *J. Phys. Chem. C*, **121**, 3286 (2017).
65. S. Ahmed et al., *ACS Nano*, **13**, 10694 (2019).
66. P. Li, Y. Zhao, Y. Shen, and S.-H. Bo, *J. Phys. Energy*, **2**, 022002 (2020).
67. S. Watanabe, M. Kinoshita, T. Hosokawa, K. Morigaki, and K. Nakura, *J. Power Sources*, **258**, 210 (2014).
68. J. Yang, B. Huang, J. Yin, X. Yao, G. Peng, J. Zhou, and X. Xu, *J. Electrochem. Soc.*, **163**, A1530 (2016).
69. S. H. Jung, U.-H. Kim, J.-H. Kim, S. Jun, C. S. Yoon, Y. S. Jung, and Y.-K. Sun, *Adv. Energy Mater.*, **10**, 1903360 (2019).
70. S. Schweidler, P. Hartmann, T. Brezesinski, and J. Janek, *Batteries & Supercaps* (2020).
71. S. Oswald, D. J. Pritzl, M. Wetjen, and H. Gasteiger, *J. Electrochem. Soc.*, **167** 100511 (2020).
72. M. D. Radin, S. Hy, M. Sina, C. Fang, H. Liu, J. Vinckeviciute, M. Zhang, M. S. Whittingham, Y. S. Meng, and A. van der Ven, *Adv. Energy Mater.*, **7**, 1602888 (2017).
73. H. Li, A. Liu, N. Zhang, Y. Wang, S. Yin, H. Wu, and J. R. Dahn, *Chem. Mater.*, **31**, 7574 (2019).
74. P.-C. Tsai, B. Wen, M. Wolfman, M.-J. Choe, M. S. Pan, L. Su, K. Thornton, J. Cabana, and Y.-M. Chiang, *Energy Environ. Sci.*, **11**, 860 (2018).
75. M. Doyle, T. F. Fuller, and J. Newman, *J. Electrochem. Soc.*, **140**, 1526 (1993).
76. W. Zhang, F. H. Richter, S. P. Culver, T. Leichtweiss, J. G. Lozano, C. Dietrich, P. G. Bruce, W. G. Zeier, and J. Janek, *ACS Appl. Mater. Inter.*, **10**, 22226 (2018).
77. F. Strauss, T. Bartsch, L. de Biasi, A.-Y. Kim, J. Janek, P. Hartmann, and T. Brezesinski, *ACS Energy Lett.*, **3**, 992 (2018).
78. D. Ren, E. Padgett, Y. Yang, L. Shen, Y. Shen, B. D. A. Levin, Y. Yu, F. J. DiSalvo, D. A. Muller, and H. D. Abruña, *ACS Appl. Mater. Inter.*, **11**, 41178 (2019).